ELSEVIER

Contents lists available at ScienceDirect

Chemical Engineering Journal

journal homepage: www.elsevier.com/locate/cej





Tunable coffee-ring patterns of sessile suspension droplets through silica particle encapsulation with thermo-responsive block copolymers

Seong Hwan Kim ^{a,1}, Yoon Huh ^{a,1}, Baek Sung Park ^a, Kevin Injoe Jung ^a, You-Yeon Won ^{b,*}, Joona Bang ^{a,*}, Hyun Wook Jung ^{a,*}

ARTICLE INFO

Keywords:
Coffee-ring effect
PMMA-b-PNIPAM block copolymer
Silica particles
Droplet drying
Thermo-responsive polymer
Multi-speckle diffusing wave spectroscopy

ABSTRACT

Silica (Si) particles coated with poly(methyl methacrylate-*b-N*-isopropylacrylamide) (PMMA-*b*-PNIPAM) block copolymers (Si-PM-PN particles) were engineered to mitigate the coffee-ring effect (CRE) frequently encountered during the drying process of particulate suspensions. Leveraging the thermo-responsive transition between the hydrophilic and hydrophobic states of PNIPAM, with its lower critical solution temperature (LCST) around 32 °C, enabled precise adjustment of the CRE. Through microrheological analysis using multi-speckle diffusing wave spectroscopy and observation under an optical microscope, the dynamic behaviors of Si-PM-PN particles in sessile suspension droplets during drying were scrutinized both below and above the LCST. Above the LCST, the Si-PM-PN particles exhibited hydrophobic characteristics, with some migrating toward the center along the droplet interface, resulting in a more uniform particle distribution post-drying. Conversely, below the LCST, the homogeneously dispersed Si-PM-PN particles displayed rapid Brownian motion, contributing to a pronounced CRE. This approach, involving the surface treatment of particles with thermo-responsive polymers, effectively altered the droplet pattern by modulating particle interactions with the air—water interface.

1. Introduction

Inkjet printing of particulate suspensions is essential for manufacturing various electronic devices, including inorganic thin films and patterned functional nanoparticles or quantum dots for displays. This process involves the dissolution or dispersion of functional materials, jetting, drying, and UV or heat curing [1,2,3,4,5]. However, colloidal particles tend to migrate during solvent evaporation, leading to non-uniform particle distribution, commonly known as the coffee-ring effect (CRE) [6,7]. This effect manifests as a concentrated accummulation of particles at the edge of a sessile suspension droplet. As the solvent evaporates faster at the droplet edge due to its larger surface area per unit volume, capillary flow occurs, drawing solvent from the center toward the edge. Consequently, particles are carried outward by this flow and aggregate at the periphery, resulting in an irregular ring-like particle structure upon drying. This unintended particle arrangement can compromise the quality of the final coating products.

Various methods have been proposed to mitigate the CRE during

suspension drying. These include: (i) preventing contact line pinning with superhydrophobic surfaces or electrowetting [8,9,10,11,12,13], (ii) disturbing capillary flow towards the contact line using Marangoni flow or electroosmosis [14,15,16,17,18], and (iii) impeding solute particle transport to the contact line by modulating interfacial interactions between particles or between particles and interfaces [19,20,21,22]. Among these approaches, adjusting interfacial interactions is particularly versatile as it does not rely on external forces. Surface-modified particles are especially effective in this regard, as the affinity of particles to adjacent particles or the air–water interface can be altered by the properties of the functional materials attached to the particle surface, thereby influencing the final droplet patterns [23].

Amphiphilic block copolymers (BCPs) present promising options for treating particle surfaces due to the inherent stability of self-assembled BCP structures [24,25,26]. Moreover, encapsulating particles with amphiphilic BCPs is straightforward using the solvent exchange method, yielding BCP/particle assemblies with a hydrophobic core and a hydrophilic shell [27,28]. Several BCP/particle hybrids, such as poly

^a Department of Chemical and Biological Engineering, Korea University, Seoul 02841, Republic of Korea

b Davidson School of Chemical Engineering, Purdue University, West Lafayette, IN 47907, United States

^{*} Corresponding authors.

 $[\]textit{E-mail addresses: } yywon@purdue.edu (Y.-Y. Won), joona@korea.ac.kr (J. Bang), hwjung@grtrkr.korea.ac.kr (H.W. Jung). \\$

¹ These authors equally contributed to this work.

(ethylene oxide)-poly(n-butyl acrylate)/Au nanorods [27], poly (ethylene glycol)-poly(n-butyl acrylate)/CaWO $_4$ nanoparticles [29], and poly(lactic acid)-poly(ethylene glycol)/Fe $_3$ O $_4$ nanoparticles [30], have been successfully prepared using this technique. Furthermore, stimulus-responsive BCPs, including thermo-, pH-, or light-responsive variants, have been employed to encapsulate particles, such as poly(ethylene oxide)-poly(trans-N-(2-ethoxy-1, 3-dioxan-5-yl) acrylamide)/fluorescein isothiocyanate-lysozyme [31] and poly(styrene)-poly(4-vinylpyridine)/Au nanoparticles [32]. However, the majority of these BCP/nanoparticle assemblies have been applied in drug delivery or diagnostic applications, with limited focus on particulate suspension coatings, which is the main focus of our study.

Poly(*N*-isopropylacrylamide) (PNIPAM), composed of hydrophilic amide and hydrophobic isopropyl groups, exhibit remarkable thermoresponsive behavior [33]. Below its lower critical solution temperature (LCST) of approximately 32 °C, PNIPAM displays hydrophilic characteristics and remains in a coil state, while above the LCST, it transitions to a hydrophobic state and adopts a globular conformation [34,35]. PNIPAM microgels, in particular, exhibit unique behavior during suspension evaporation; their amphiphilic nature leads to the adsorption at the air–liquid interface, altering particle coating patterns away from typical coffee-ring depositions [36,37,38,39]. Despite these observations, the potential of PNIPAM's thermo-responsive properties for modulating the CRE remains largely unexplored. Therefore, leveraging PNIPAM as the outer shell of BCP/particle assemblies could offer an effective approach to controlling the drying dynamics of sessile suspension droplets in inkjet coating processes.

In this study, we employ particles coated with thermo-responsive BCPs to regulate the drying pattern of particle suspensions via temperature modulation. Initially, silica (Si) particles were encapsulated within a poly(methyl methacrylate-b-N-isopropylacrylamide) (PMMA-b-PNI-PAM) BCP shell formed through a solvent exchange process, yielding Si-PM-PN particles. The encapsulation of Si particles with BCPs and the thermo-responsive behavior of Si-PM-PN particles in colloidal suspensions were validated using transmission electron microscopy (TEM), dynamic light scattering (DLS), and surface tension measurements using a tensiometer. Changes in the mobility of Si-PM-PN particles at different time scales during suspension drying, influenced by the thermoresponsive properties of the PNIPAM chains, were monitored via multi-speckle diffusing wave spectroscopy (MSDWS) under various temperature conditions. Furthermore, the movement of Si-PM-PN particles within a sessile droplet during drying was observed using an optical microscope. The resultant particle arrangement after suspension drying was examined using scanning electron microscopy (SEM) and a noncontact surface profiler.

2. Materials and methods

2.1. Synthesis of PMMA-b-PNIPAM block copolymers

The PMMA-b-PNIPAM block copolymer was synthesized via reversible addition-fragmentation chain-transfer (RAFT) polymerization, as illustrated in Fig. 1 [40,41]. The molecular weights and block proportions of the components in PMMA-b-PNIPAM were tailored to ensure

stable coverage on particle surfaces and to exhibit notable thermoresponsive behaviors [42,43]. Initially, a mixture of methyl methacrylate (MMA, monomer, MW = 100.121 g/mol, DAEJUNG, Siheung-si, Republic of Korea), 2,2'-azobis(isobutyronitrile) (AIBN, radical initiator, MW = 164.21 g/mol, Sigma-Aldrich, St. Louis, MO, USA), 4-cyano-4(phenylcarbonothioylthio)pentanoic acid (CPCP, RAFT agent, MW = 279.38 g/mol, Sigma-Aldrich, St. Louis, MO, USA), and toluene (DAE-JUNG, Siheung-si, Republic of Korea) was prepared in a reaction vessel. The molar ratio of the monomer, radical initiator, and RAFT agent was set to 200/0.1/1, with the mass of toluene equivalent to that of the MMA monomer. The vessel was sealed using a latex stopper with two needles installed for gas substitution, and then filled with Ar gas through the inlet needle. Subsequently, the vessel was heated to 70 °C, and the mixture was stirred for 2 h and 15 min. After the reaction, the PMMA-RAFT was precipitated in cold hexane (DAEJUNG, Siheung-si, Republic of Korea) and then dried in a vacuum oven (OV-01, Jeio Tech, Daejeon, Republic of Korea). The resulting PMMA-RAFT was analyzed by gel permeation chromatography (GPC, Waters 1515 pump, Water 2414 refractive index detector, Waters Corp., Milford, MA, USA), yielding a number-average molecular weight (Mn) of 4,000 g/mol and a polydispersity index (PDI) of 1.11 (Table 1).

Subsequently, *N*-isopropylacrylamide (NIPAM, MW = 113.16 g/mol, Sigma-Aldrich, St. Louis, MO, USA) was added to the ends of the PMMA-RAFT chains. NIPAM, AIBN, and PMMA-RAFT were dissolved in toluene at a molar ratio of 200/0.1/1 in a reaction vessel filled with Ar gas. The vessel was then heated to 80 °C using an oil bath, and the mixture was stirred for 36 h. After the reaction, the resulting PMMA-b-PNIPAM-RAFT copolymer was precipitated in cold diethyl ether (DAEJUNG, Siheung-si, Republic of Korea) and subsequently dried under vacuum. Finally, the RAFT end groups were removed by reacting with an excess amount of AIBN. The M_n and PDI of the final PMMA-b-PNIPAM (PM-PN) BCP were determined to be 11,500 g/mol and 1.09, respectively, using GPC (Table 1). The molar ratio between the PMMA and PNIPAM blocks in the PM-PN BCP was confirmed to be 1:2 through ¹H nuclear magnetic resonance (NMR) spectroscopy (500 MHz FT-NMR spectrometer, Bruker, Billerica, MA, USA) (Fig. 2), consistent with the GPC results (Table 1). The temperature-dependent behaviors of PM-PN BCPs in water were investigated in the form of micelles, and detailed experimental methods and results are provided in Sections S1.1 and S1.2 of the Supplementary Material.

2.2. Encapsulation of silica particles with PMMA-b-PNIPAM block copolymers through solvent exchange

2.2.1. Determining solvent composition for the solvent exchange method For the solvent exchange method, DI water and acetone (DAEJUNG,

 $\begin{tabular}{ll} \textbf{Table 1} \\ \textbf{Number-average molecular weight } (M_n) \ and \ polydispersity index \ (PDI) \ of PMMA-RAFT and PMMA-b-PNIPAM. \end{tabular}$

Property	PMMA-RAFT	PMMA-b-PNIPAM
M _n (g/mol)	4,000	11,500
PDI (M_w/M_n)	1.11	1.09

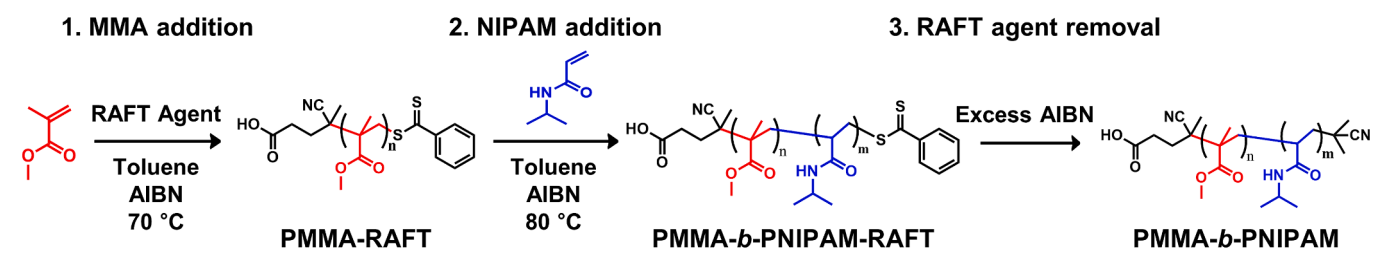


Fig. 1. Schematic representation of PMMA-b-PNIPAM synthesis via RAFT polymerization.

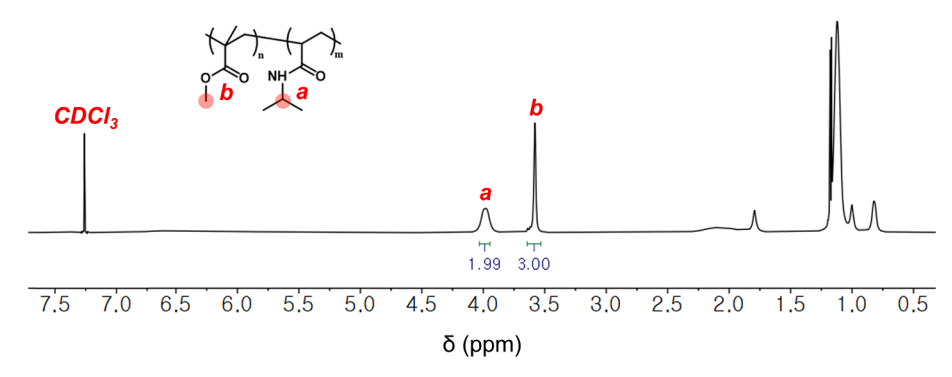


Fig. 2. ¹H NMR spectra of synthesized PMMA-b-PNIPAM.

Siheung-si, Republic of Korea) were chosen to facilitate the formation of an encapsulating PM-PN layer, with inner PMMA segments and outer PNIPAM segments. This choice was made because PMMA is soluble only in acetone, while PNIPAM is soluble in both solvents. To determine the suitable range of solvent compositions for the formation of PM-PN BCP assemblies or micelles, samples were prepared by dissolving 0.06 g of PM-PN BCPs in acetone, followed by the gradual addition of water. The total volume of the solvent mixture was 3 mL, and the volume fraction of water varied from 0.1 to 0.9. Subsequently, the samples' apparent states were observed, and the hydrodynamic diameters of the PM-PN BCPs in the solvent mixtures were measured using DLS (BI-200SM, Brookhaven Instruments, Holtsville, NY, USA) after dilution with a solvent mixture of the same composition [27], as illustrated in Fig. 3. It was verified that PM-PN BCP assemblies or micelles were formed between 0.5 and 0.9 of the water volume fraction for 0.06 g of PM-PN BCPs in a 3 mL water/ acetone mixture.

2.2.2. Encapsulation of silica particles via the solvent exchange method Si particles with a diameter of 1 μm (NanoCym, Scottsdale, AZ, USA)



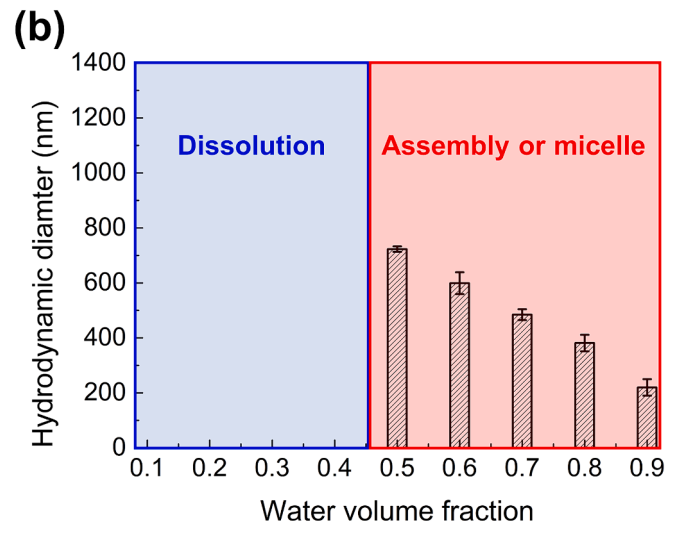


Fig. 3. (a) Apparent states and (b) hydrodynamic diameter results of PMMA-*b*-PNIPAM in water–acetone mixture as a function of water volume fraction.

were encapsulated with PM-PN BCPs through a self-assembly process driven by solvent exchange using water and acetone (7:3 volume ratio of solvent mixture) as the solvent medium, as depicted in Fig. 4 [27,28]. Initially, 0.06 g of PM-PN BCPs were added to 0.9 mL of acetone to prepare the PM-PN BCP solution, and 0.02 g of Si particles were dispersed in the solution using an ultrasonic processor (VC-505, Sonics and Materials, Newtown, CT, USA). Subsequently, 2.1 mL of DI water was slowly added to the mixture at a rate of 0.05 mL/min under magnetic stirring at 1,200 rpm. Following the addition of DI water, the mixture was sonicated with an ultrasonic processor for 30 min in a cooling bath and then stirred with a magnetic bar at 1,200 rpm for 4 h. The resulting Si particles encapsulated with PM-PN BCPs (Si-PM-PN particles) underwent purification through a centrifugation process, followed by re-dispersion in DI water and centrifugation again to remove any residual PM-PN BCP assemblies. Finally, the Si-PM-PN particles were dispersed in DI water to obtain a suspension of 3 wt%. It is noteworthy that the concentration of the Si-PM-PN suspension was determined based on the initially added mass of Si particles, focusing solely on the encapsulating BCP layer, in comparison with a Si suspension with the same concentration of 3 wt%, as outlined in detail in Table 2. The experimental methods and results for characterizing the Si-PM-PN particles are described in Sections S2.1 and S2.2 of the Supplementary Material.

2.3. Temperature-dependent behavior of Si-PM-PN particles in suspension

2.3.1. Hydrodynamic diameters of Si and Si-PM-PN particles in suspensions

To explore the temperature-dependent behavior of the Si-PM-PN particles in an aqueous medium, the hydrodynamic diameters of both the Si and Si-PM-PN particles were measured multiple times at 25 and 40 °C, representing temperatures below and above LCST, respectively. DLS was employed for measurements including DLS intensity correlation functions, while ensuring a single scattering event by diluting the samples. For measurements at 40 °C, the sample was heated and then diluted before analysis. Also, the size anlysis of the Si-PM-PN particles near the LCST of PNIPAM was conducted, with detailed results described in Section S3 of the Supplementary Material.

2.3.2. Microstructures in Si and Si-PM-PN suspensions

The microstructures in the Si and Si-PM-PN suspensions at 25 and 40 $^{\circ}$ C were examined using TEM (Tecnai 20, FEI, Hillsboro, OR, USA) and correlated with the hydrodynamic diameter measurements. Diluted samples, identical to those used for the hydrodynamic diameter measurements, were deposited onto plasma-cleaned TEM grids and allowed to dry under atmospheric conditions.

2.3.3. Real-time surface tension measurement of Si and Si-PM-PN suspensions with changing temperature

The surface tensions of the Si and Si-PM-PN suspensions were



1. Addition of water 2. Sonication 3. Magnetic stirring 4. Purification 5. Re-dispersion

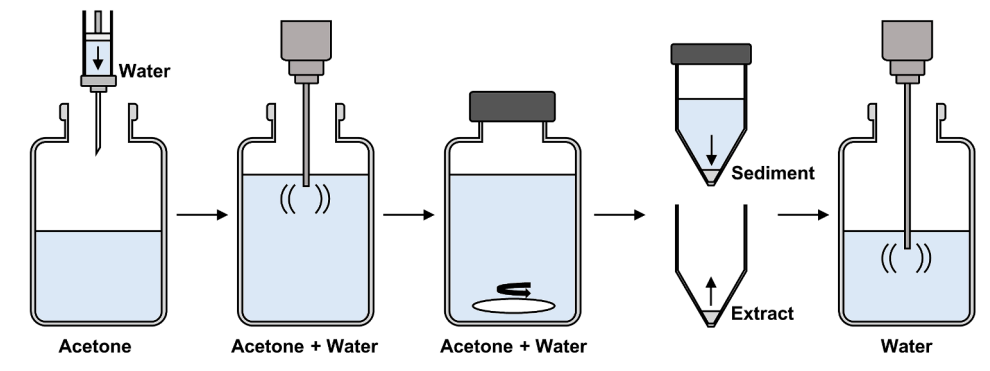


Fig. 4. Schematic illustration of encapsulating Si particles with PMMA-b-PNIPAM using solvent exchange method.

Table 2 Formulations of Si and Si-PM-PN particle suspensions.

Suspension	Si	Si-PM-PN
Si particle (g)	0.02	0.02
PM-PN BCP (g)	_	0.0584
DI water (g)	0.64	0.64
Concentration (wt%, with respect to Si particle)	3	3

measured in real-time by varying the temperature using a tensiometer (DCAT11, Data Physics, Filderstadt, Germany) equipped with a thermoplate (TPi-SX, Tokai Hit, Fujinomiya, Japan). A platinum-iridium plate measuring 10 mm in length, 19.9 mm in width, and 0.2 mm in thickness was immersed in the samples at 25 °C for 240 s. The temperature was then increased to 40 °C at a rate of 0.3 °C/s for 50 s and maintained for 1,510 s. Surface tension was measured every 0.2 s throughout the 1,800 s duration, and the measurement was repeated several times to ensure the reliability of the data.

2.4. Characterization of Si and Si-PM-PN particle motions in suspension droplets during drying using multi-speckle diffusing wave spectroscopy (MSDWS)

2.4.1. Measurement of particle motion with MSDWS

Particle mobility was analyzed using MSDWS on both short (less than 10^{-1} s) and long time scales (greater than 10^{0} s), and the analysis were repeated several times to ensure the robustness of data [44,45]. For MSDWS measurements, 1 µL sessile droplets of the Si and Si-PM-PN suspensions were deposited on a glass substrate and maintained at temperatures of 25 and 40 °C during drying under a constant relative humidity of 33 %. The droplets were illuminated with light from a temperature-stabilized laser (DPGL-2200, Jinsung Laser, Daejeon, Republic of Korea) with a wavelength of 532 nm, an output power of 200 mW, a beam diameter of 1 mm, and the TEM00 beam mode. The scattered light was captured using two types of cameras: a CMOS line scan camera and a charge-coupled device (CCD), allowing investigation of particle motions on short (β -relaxation) and long time (α -relaxation) scales, respectively. The CMOS line scan camera (spL-4096-39 km, Basler Vision Technologies, Ahrensburg, Germany) with a frame rate of 38.6 kHz provided a speckle line image of 4,096 pixels. Temporal lines with a time interval of 26 µs were aligned vertically to form images of $4,096 \times 4,096$ pixels for a lag time of 0.1 s. Conversely, a CCD (Prosilica GC1290C, Allied Vision, Stadtroda, Germany) with a frame rate of 33 Hz captured speckle images comprising 960 \times 1,280 pixels with a time interval of 0.03 s. Note that speckle image patterns were more influenced by the mobility of particles near the top surface of a sessile droplet due to the nature of this speckle interferometry technique [46]. The images obtained from the CMOS line scan camera and CCD were interpreted using the autocorrelation function and the inertia moment of the matrix [46,47,48,49], respectively.

2.4.2. Interpretation of fast Brownian motion using autocorrelation function

The fast Brownian motion, known as β -relaxation, of particles in suspension droplets during drying plays a critical role in determining the final droplet patterns. Speckle images captured with a CMOS line scan camera in a short lag time allow for the qualitative analysis of fast Brownian motion using the autocorrelation function $(g_2 - 1)$, as defined in Eq. (1).

$$g_2(t_w, \tau) - 1 = \frac{\langle I_n(t_w + \tau)I_n(t_w)\rangle_n}{\langle I_n(t_w + \tau)\rangle_n \langle I_n(t_w)\rangle_n} - 1 \tag{1}$$

Here, I_n represents the light intensity at the n-th pixel, $\langle \cdots \rangle_n$ denotes the ensemble average over the pixels, and t_w and τ denote the drying time and lag time, respectively. g_2-1 in Eq. (1) at each drying time was normalized to achieve an initial value of unity.

2.4.3. Analysis of particle mobility on long time scales using the inertia moment of the matrix

The transient variation of particle motion on long time scales, known as $\alpha\text{-relaxation},$ during drying is crucial as it relates to the structural rearrangements of particles, which are challenging to analyze on short time scales ($\beta\text{-relaxation})$ [44]. Particle motion over long time scales can be interpreted using the inertia moment (IM) of the matrix [46,47,48,49]. Initially, the center row, comprising 1,280 pixels in each speckle image captured by a CCD at intervals of 0.03 s, was selected as representative data for the corresponding capture time. These representative rows were then aligned in the vertical direction for 5 s to form images comprising $165 \times 1,280$ pixels at each capture time. The pixels were converted to digits from 0 to 255 based on their brightness, and the co-occurrence matrix (COM) was formed, as shown in Eq. (2)

$$COM = [N_{ij}] (2)$$

Here, N_{ij} represents the number of occurrences of brightness value i at a pixel in all rows, except the last row, and the brightness value j at a pixel in the same column in the next row of the speckle image of 165 \times 1,280

pixels. If the particles exhibit higher mobility, the diagonal terms in the COM become less crowded. For convenience, the COM was normalized by dividing the value in each row by the sum of the corresponding rows to form a modified COM (MCOM), as shown in Eq. (3)

$$MCOM = M_{ij} = \frac{N_{ij}}{\sum_{i} N_{ij}}$$
 (3)

The distribution of M_{ij} with respect to the diagonal terms in the MCOM can be interpreted using IM, as in Eq. (4).

$$IM = \sum_{ij} M_{ij} (i-j)^2 \tag{4}$$

The IM values during drying were normalized from 0 to 1 using Eq. (5). If the transient variation in particle motion is significant, the normalized IM (IM₀) approaches unity.

$$IM_0 = \frac{IM_t - IM_{min}}{IM_{max} - IM_{min}} \tag{5}$$

2.5. Observation of Si and Si-PM-PN suspension sessile droplets during and after drying

2.5.1. Observation of Si and Si-PM-PN sessile suspension droplet edges during drying

To observe particle movement in a sessile droplet during drying, 1 μL sessile droplets of the dilute Si and Si-PM-PN suspensions (0.15 wt%) were placed on a glass substrate, where the temperature was controlled using a thermoplate (TPi-SX, Tokai Hit, Fujinomiya, Japan). The edges of the droplets were observed using an optical microscope (MCX500, Micros Austria, Gewerbezone, Austria). The temperature and relative humidity were maintained at the same values as those described in Section 2.4.1.

2.5.2. Dried patterns of Si and Si-PM-PN sessile suspension droplets

 $1~\mu L$ sessile droplets of the Si and Si-PM-PN suspensions (3 wt%) were deposited onto the glass substrate, and the substrate was then placed on the hot plate to maintain the specified temperature during drying under a constant relative humidity condition, as described in Section 2.4.1. The dried droplet patterns were observed using SEM (S-4800, Hitachi, Tokyo, Japan) and their 2-D profiles were obtained using a non-contact surface profiler (Contour GT-K, Bruker, Billerica, MA, USA).

3. Results and discussion

3.1. Temperature-dependent behaviors of Si and Si-PM-PN particles in suspension

3.1.1. Microstructures in Si and Si-PM-PN suspensions

Surface modification of Si particles with PM-PN BCPs was achieved through a solvent exchange method. This method leverages the interplay between two factors: (i) the tendency of PM-PN BCPs to form micelles due to the low solubility of PMMA in water, and (ii) hydrogen bonding between the carbonyl group (C = O) in PMMA and the silanol group (-SiOH) on the Si particle surface [50,51]. This process resulted in Si-PM-PN particles with thermo-responsive properties akin to PNI-PAM (Figs. S1, S2, and S5). Fig. 5 depicts the hydrodynamic diameters of Si and Si-PM-PN particles measured at 25 and 40 °C using DLS, along with TEM observations of their microstructures. Note that the sample at 40 °C was prepared through heating and subsequent dilution. In the Si suspension, particles consistently exhibited a hydrodynamic diameter of approximately 1 µm with a narrow distribution (Fig. 5a). This diameter remained unchanged across temperatures, consistent with the rapid decay of the intensity correlation function at the early lag time (Fig. S6). TEM imaging revealed a clean particle surface (Fig. 5c). Conversely, in the Si-PM-PN suspension at 25 $^{\circ}$ C, the hydrodynamic diameter was

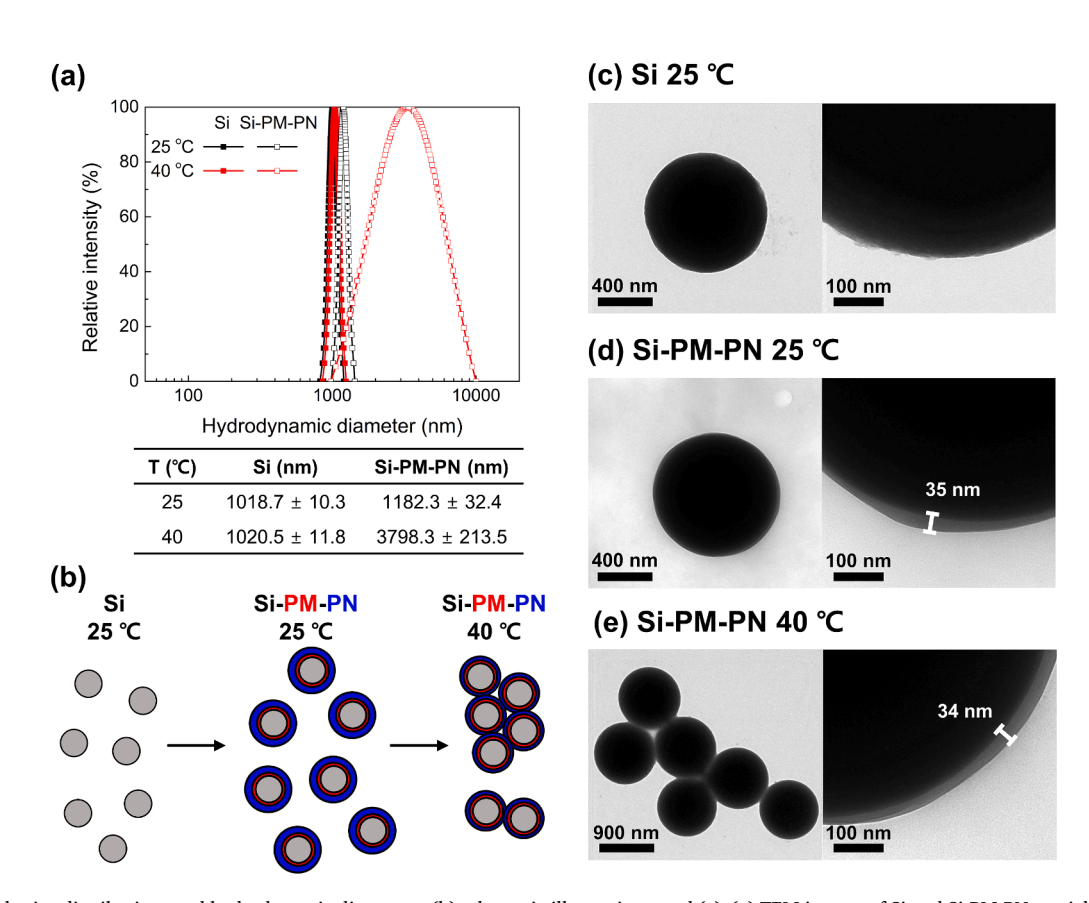


Fig. 5. (a) Particle size distributions and hydrodynamic diameters, (b) schematic illustrations, and (c)–(e) TEM images of Si and Si-PM-PN particles at 25 and 40 °C. The sample for 40 °C was prepared by heating and subsequent dilution.

slightly larger and exhibited a narrow distribution, approximately 1.2 μm (Fig. 5a). This corresponds to the rapid decay of the intensity correlation function at a slightly later lag time (Fig. S6). This slight increase in diameter could be attributed to the homogeneous encapsulating PM-PN BCP layer (Figs. 5d, S3, and S4). The hydrophilic amide group of PNIPAM fostered interactions with water molecules via hydrogen bonding, resulting in a well-dispersed Si-PM-PN suspension. Upon increasing the temperature to 40 °C, surpassing the LCST of PNIPAM, the hydrodynamic diameter notably increased, accompanied by a significantly broader distribution (Fig. 5a). Additionally, the intensity correlation function started to decay slowly at a much later lag time (Fig. S6). This phenomenon occurred due to aggregation of some Si-PM-PN particles via hydrophobic interactions arising from the coil-to-globule transition of the PNIPAM chains, disrupting hydrogen bonding between water and the amide group (Figs. 5b and 5e) [52]. Notably, shrinkage of the PM-PN BCP coating layer was negligible (Fig. 5e). This observation is comparable to the layer at 25 $^{\circ}$ C (Fig. 5d), because TEM imaging was conducted in the dried state under vacuum [53,54].

3.1.2. Air-water interfacial activity of Si and Si-PM-PN particles in suspension

To investigate the impact of the thermo-responsive PNIPAM layers on the air-water interfacial activity of Si-PM-PN particles in suspension, real-time measurements of surface tensions were conducted for DI water, 3 wt% Si suspension, and 3 wt% Si-PM-PN suspension with changing temperature, and comparisons were made (Fig. 6). For DI water, the surface tension slightly decreased from 72 to 70 mN/m as the temperature increased from 25 to 40 °C due to the weakening of cohesive forces caused by volume expansion from higher molecular thermal activity [55]. Similarly, the Si suspension displayed a comparable surface tension behavior, indicating that particles were not predominantly present at the air-water interface. However, in the case of the Si-PM-PN suspension, the surface tension value was initially lower and continued to decrease as the temperature rose to 40 $^{\circ}$ C. This suggests that Si-PM-PN particles moved and were adsorbed at the air-water interface above the LCST of PNIPAM [56,57]. The adsorption of particles originates from the strong affinity of the hydrophobic PNIPAM chains for the air-water interface [58].

3.2. Drying behavior of Si and Si-PM-PN sessile suspension droplets as a function of temperature

3.2.1. Dynamics of Si and Si-PM-PN particles during drying of suspension droplets on short time scales

Particle mobility for 1 μ L-sized 3 wt% Si and Si-PM-PN suspension

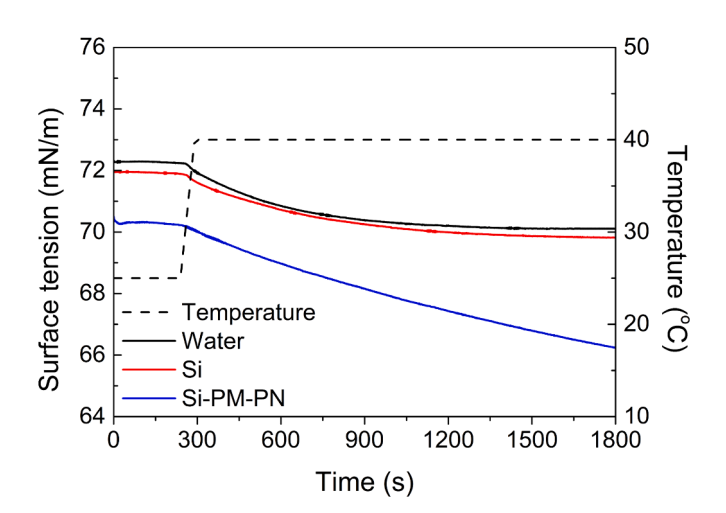


Fig. 6. Real-time surface tension variations of water, 3 wt% Si, and 3 wt% Si-PM-PN suspensions with changing temperature.

droplets during drying on short time scales was assessed using MSDWS and qualitatively analyzed using an autocorrelation function, as depicted in Figure S7. To compare them, the characteristic time, when the autocorrelation function curve for each drying time decreased to 0.6, was plotted (Fig. 7) [44,59,60]. With increasing drying time, the autocorrelation functions gradually decreased, and the characteristic time increased accordingly due to solvent evaporation, constraining the space for rapid particle movement. Towards the end of the drying stage, the autocorrelation function remained at a constant value of unity, indicating particle jamming due to solvent removal.

At 25 °C, the Si-PM-PN particles exhibited relatively lower mobility than that of the Si particles (Figs. S7a and S7c), evident from the higher characteristic time values in the Si-PM-PN suspension droplet (Fig. 7). This was primarily attributed to the encapsulating BCP layer on the Si-PM-PN particle, which increased particle size and reduced mobility (Figs. 5a and 5d). At 40 °C, the autocorrelation function decreased more rapidly during the early drying stage, and lower characteristic times were measured in both suspension droplets compared to those at 25 °C (Figs. S7b and S7d). This acceleration was due to the high substrate temperature inducing greater thermal motion of the particles initially. Additionally, Si-PM-PN particle mobility was slightly lower than that of Si particles during drying. Besides the encapsulating BCP layer, some Si-PM-PN particle aggregates, formed due to hydrophobic interactions at temperatures above the LCST of PNIPAM (Figs. 5a, 5e, and S5), can be considered an additional factor reducing mobility. However, if the aggregates sediment during drying, the autocorrelation functions for the Si-PM-PN droplet at 40 °C would decay much slower [59]. Thus, when considering that the characteristic times of the Si-PM-PN particles at both 25 °C and 40 °C increased at the same ratio compared to those of the Si particles (Fig. 7), it is reasonable that the particle behavior in the Si-PM-PN suspension droplet at 40 °C was not primarily influenced by sedimentation.

3.2.2. Dynamics of Si and Si-PM-PN particles during drying of suspension droplets on long time scales

The temporal evolution of particle motion in 1 μ L-sized 3 wt% Si and Si-PM-PN suspension droplets during drying over long time scales was delineated by IM₀ patterns, as depicted in Fig. 8. Two distinct drying phases emerge from these patterns: the compacting and air-invading stages [49]. During the compacting stage, the IM₀ value escalated with drying progression due to the particles exhibiting swift motion propelled by intensified capillary flow [61,62,63]. Conversely, in the air-invading stage, solvent flow to the menisci in small pores becomes

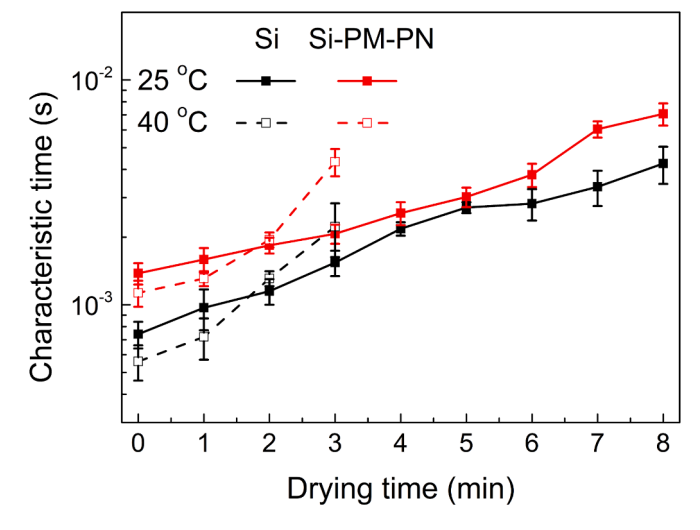


Fig. 7. Characteristic times, when the autocorrelation functions decreased to 0.6, for 1 μL -sized 3 wt% Si and Si-PM-PN suspension droplets during drying at 25 $^{\circ}C$ and 40 $^{\circ}C$.

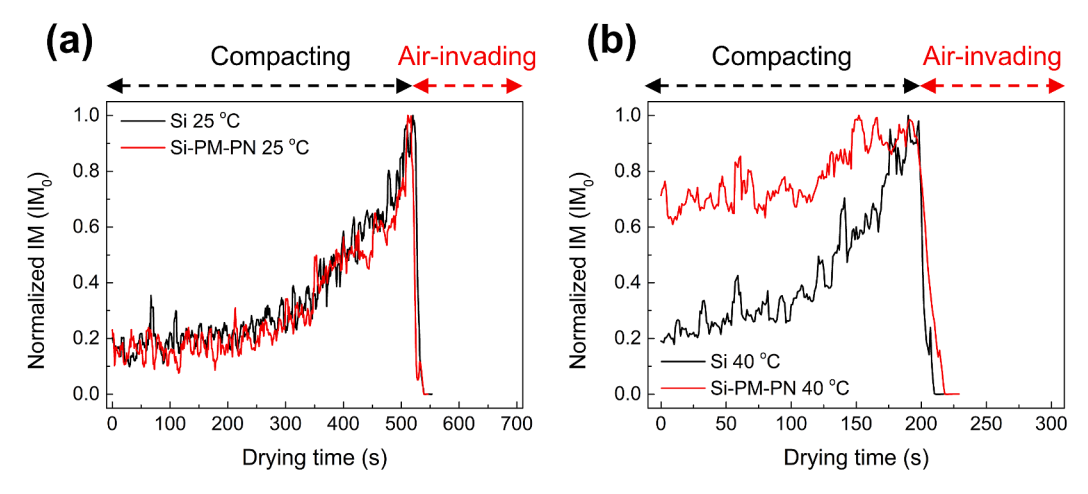


Fig. 8. Normalized inertia moment (IM₀) of the matrix of 1 µL-sized 3 wt% Si and Si-PM-PN suspension droplets during drying at (a) 25 °C and (b) 40 °C.

dominant owing to capillary pressure [64,65,66]. Consequently, the IM₀ value rapidly decreased to 0 by the absence of bulk flow. At 25 °C, during the compacting stage, IMo values for the Si-PM-PN suspension droplet mirrored those of the Si suspension droplet (Fig. 8a), indicating that particles experienced outward capillary flow in both suspensions. Notably, at 40 °C, the Si-PM-PN suspension droplet exhibited higher IM₀ values compared to the Si suspension droplet during the compacting stage (Fig. 8b), implying that Si-PM-PN particles could exhibit greater mobility over long time scales. Therefore, besides being influenced by outward flow during droplet drying, another factor might promote particle mobility. It is conceivable that in this measurement, the behavior of particles near the air-water interface played a significant role in shaping the IM₀ patterns as mentioned in Section 2.4.1. Consequently, it is plausible that at 40 °C, Si-PM-PN particles underwent rapid motion near the air-water interface, which was consistent with the surface tension measurements (Fig. 6).

3.2.3. Particle movement in Si and Si-PM-PN suspension droplets

To physically interpret particle motion and correlate the mobility of Si-PM-PN particles at 40 °C (Fig. 8b), the edges of 1 μL -sized Si and Si-PM-PN suspension droplets, diluted to 0.15 wt%, were primarily observed using an optical microscope after 3 min of drying (Supplementary Videos 1–4). For the Si suspension droplet at both 25 and 40 °C, and the Si-PM-PN suspension droplet at 25 °C, particles continuously migrated toward the droplet edge due to outward capillary flow (Supplementary Videos 1–3). However, in the Si-PM-PN suspension droplet

at 40 °C, some particle aggregates were observed to adsorb onto the air—water interface and move toward the center along the interface by inward flow, while other particles were still influenced by outward flow (Fig. 9 and Supplementary Video 4). This occurred because the adherence of particles at the air—water interface, combined with the temperature gradient, induces a large surface tension gradient along the droplet interface, which is sufficient to initiate an inward flow [15,16,18]. Consequently, this movement resulted in the high Si-PM-PN particle mobility measurement at 40 °C over long time scales (Fig. 8b). Note that high temperature alone cannot be considered the sole factor affecting droplet patterns through the induction of inward flow, such as thermal Marangoni flow [15,16], in the system. This is evidenced by the absence of inward flow observed in the Si suspension droplet at 40 °C (Supplementary Video 2).

3.2.4. Dried patterns of Si and Si-PM-PN suspension droplets

SEM images and cross-sectional 2-D profiles of the 1 μ L-sized 3 wt% Si and Si-PM-PN sessile suspension droplets dried at both 25 and 40 °C are presented in Fig. 10. For the Si suspension droplets dried at both temperatures, the CRE was pronounced due to outward capillary flow, resulting in a high edge height compared to the center height (Figs. 10a, 10b, and 10c). Additionally, in the Si-PM-PN suspension droplet dried at 25 °C, the CRE remained prominent (Figs. 10d and 10f). However, at 40 °C, the droplet pattern underwent a significant change, exhibiting a more uniform distribution (Figs. 10e and 10f). This change is attributed to increased particle migration toward the center during drying, leading

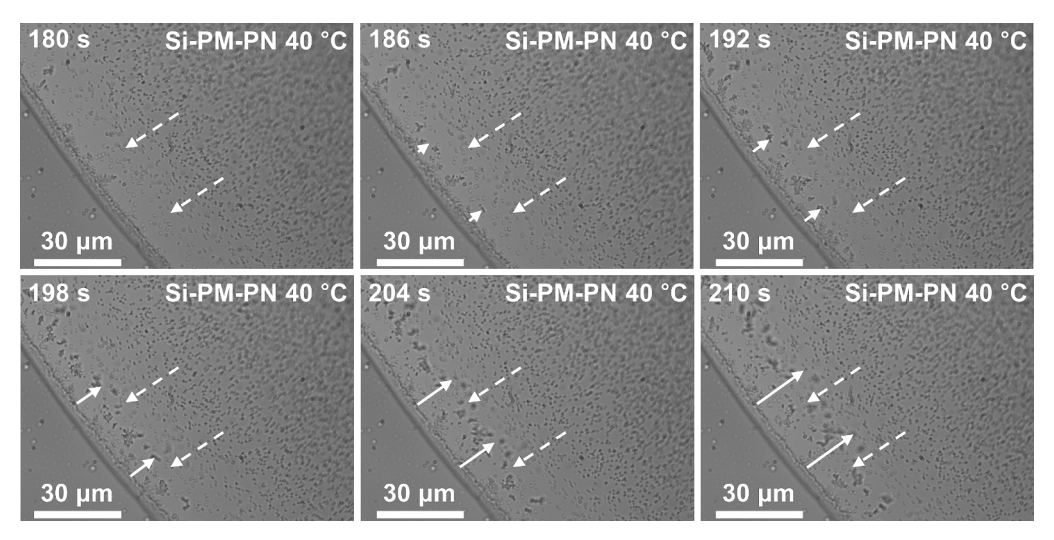


Fig. 9. Optical snapshots capturing the edges of 1 μL-sized Si-PM-PN suspension droplets during drying at 40 °C. The samples were diluted to 0.15 wt%.

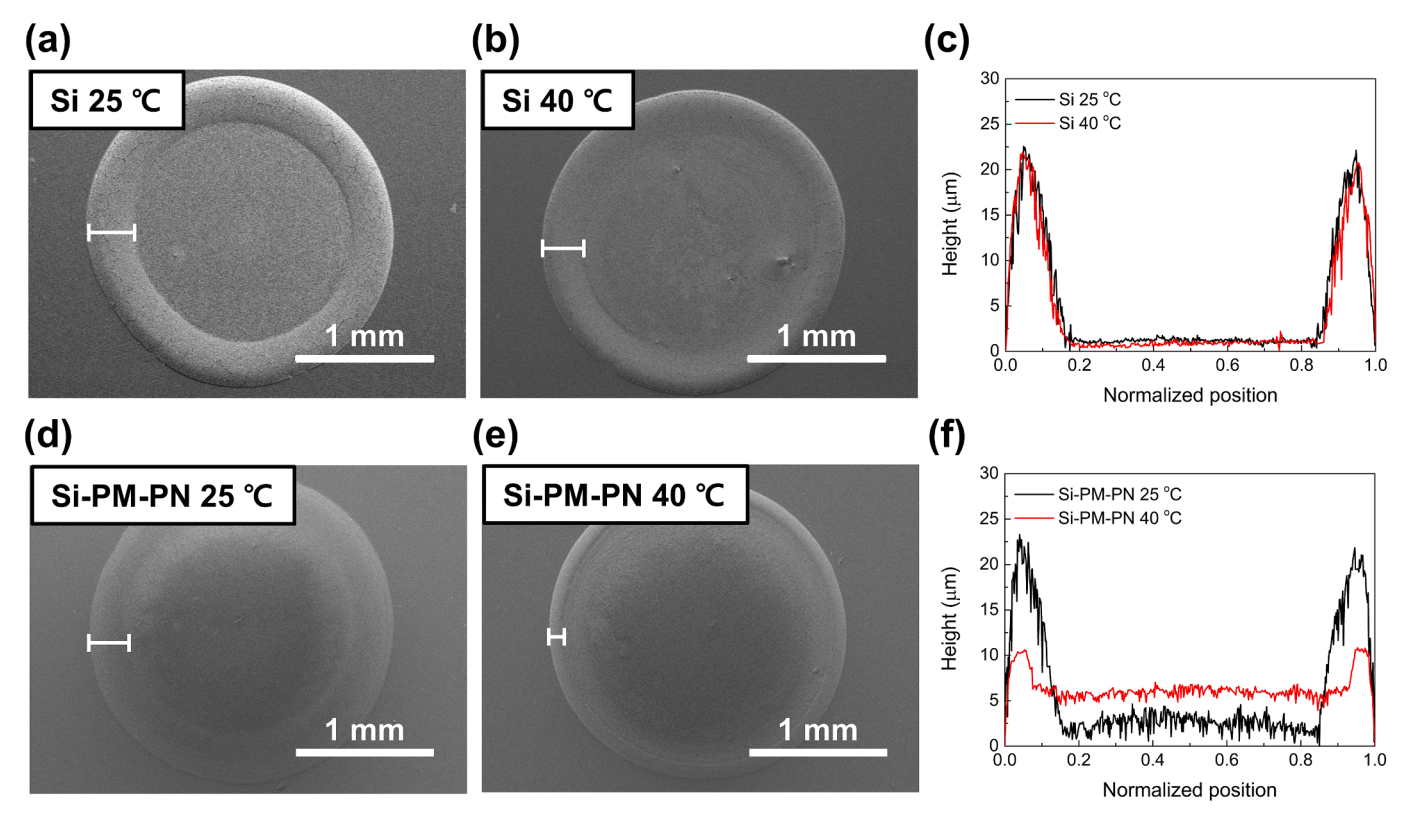


Fig. 10. SEM images capturing 3 wt% Si suspension droplets at (a) 25 °C and (b) 40 °C, along with (c) 2-D profiles of the droplets. SEM images of 3 wt% Si-PM-PN suspension droplets at (d) 25 °C and (e) 40 °C, along with (f) their respective 2-D profiles.

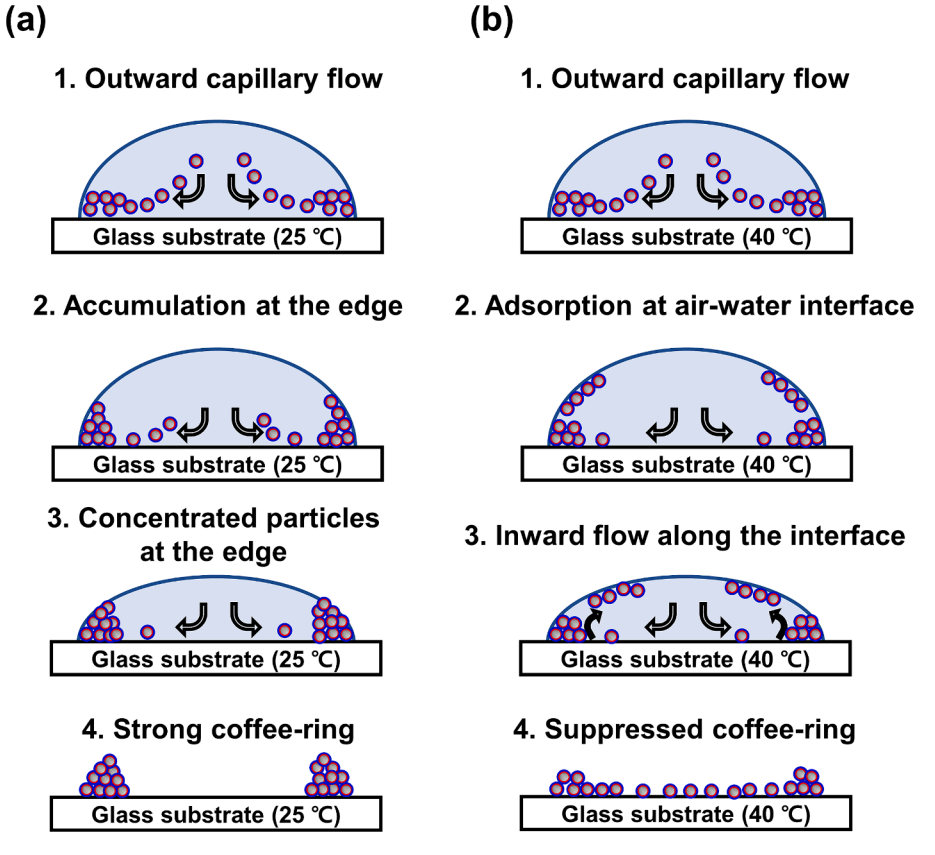


Fig. 11. Schemes depicting the drying processes of Si-PM-PN suspension droplets at (a) 25 °C and (b) 40 °C.

to an elevated height in the central region and a decreased height at the edge, as discussed in Section 3.2.3. Therefore, a high temperature above the LCST of PNIPAM induced a change in the droplet pattern due to the thermo-responsive behavior of the Si-PM-PN particles.

3.3. Mechanism of Si-PM-PN suspension droplet drying as affected by temperature

Based on drying behaviors and droplet patterns, the drying process of Si-PM-PN suspension droplets at 25 and 40 °C can be elucidated in five steps, as portrayed in Fig. 11. In the initial drying stage, particles migrated to the edge due to outward capillary flow in both cases. At this point, the thermo-responsive characteristics of the PNIPAM brushes on the Si-PM-PN particles did not significantly alter the drying behavior. At 25 °C, particle accumulation at the edge persisted until drying was complete, resulting in a pronounced coffee-ring pattern (Fig. 11a). However, at 40 °C (Fig. 11b), as more particles accumulated near the edge after sufficient drying time, the increased hydrophobicity of the PNIPAM brushes caused particles to position themselves at the air-water interface and aggregate [58]. Subsequently, a high surface tension gradient induced by the relatively high temperature and air-water interfacial particles prompted the migration of interfacial particles toward the central region along the droplet interface, while the solvent continued to evaporate during drying. Ultimately, a uniform droplet pattern emerged, deviating from the typical strong coffee-ring pattern.

4. Conclusion

Thermo-responsive Si-PM-PN particles were engineered by encapsulating Si particles with PM-PN BCPs using a solvent exchange method to tailor coffee-ring patterns. Their thermo-responsive behaviors in suspension were validated with DLS, TEM, and a tensiometer at two different temperatures (25 and 40 °C), below and above the LCST, respectively. At 40 °C, the BCP coating layer contracted, leading to aggregation of the Si-PM-PN particles, while the dispersion of Si-PM-PN particles remained uniform at 25 °C. Additionally, as the temperature increased from 25 to 40 °C, the Si-PM-PN particles were observed to adsorb onto the air-water interface by hydrophobic interactions. The drying behaviors of Si and Si-PM-PN suspension droplets at 25 and 40 $^{\circ}\text{C}$ were investigated using MSDWS. The autocorrelation functions throughout the drying process indicated that Si-PM-PN particles exhibited slower motion on short time scales due to the encapsulating layer at both temperatures. However, the inertia moment of the matrix, describing particle mobility on long time scales, revealed that Si-PM-PN particles exhibited greater movement compared to Si particles at 40 °C, suggesting additional behavior of Si-PM-PN particles near the air-water interface at this temperature. For a detailed analysis, the edge of the suspension droplet was examined using an optical microscope. At 40 °C, it was confirmed that Si-PM-PN particles adsorbed at the air-water interface due to increased hydrophobicity and migrated toward the central region along the interface due to surface tension gradients originating from the temperature and particles at the air-water interface. Consequently, the droplet pattern of the Si-PM-PN suspension transitioned from a pronounced coffee-ring pattern at 25 °C to a more uniform pattern at 40 °C. Our approach, utilizing thermo-responsive particles, holds promise for particulate suspension applications where coffee-ring patterns are undesired.

CRediT authorship contribution statement

Seong Hwan Kim: Writing – review & editing, Writing – original draft, Visualization, Methodology, Investigation, Formal analysis, Data curation. Yoon Huh: Writing – review & editing, Visualization, Methodology, Investigation, Formal analysis, Data curation. Baek Sung Park: Writing – original draft, Validation, Data curation. Kevin Injoe Jung: Writing – original draft, Validation, Data curation. You-Yeon

Won: Writing – review & editing, Resources, Project administration, Funding acquisition, Data curation, Conceptualization. **Joona Bang:** Writing – review & editing, Resources, Project administration, Investigation, Conceptualization. **Hyun Wook Jung:** Writing – review & editing, Writing – original draft, Supervision, Resources, Project administration, Investigation, Funding acquisition, Conceptualization.

Declaration of competing interest

The authors declare that they have no known competing financial interests or personal relationships that could have appeared to influence the work reported in this paper.

Data availability

Data will be made available on request.

Acknowledgements

This study received support from the Ministry of Trade, Industry, and Energy of Korea (MOTIE, Korea) under the Industrial Technology Innovation Program (No. 20011712), as well as the National Research Foundation of Korea (NRF) of the Ministry of Science and ICT (MSIT) of the Korean government (Grants No. NRF-2021M3H4A6A01041234 and No. NRF-2018R1A5A1024127), and the BK21 FOUR Program (No. 41999904144614) of the Ministry of Education (MOE, Korea) and the NRF. YYW acknowledges with gratitude the support from the US NSF (CBET-2211843)

Appendix A. Supplementary data

Supplementary data to this article can be found online at https://doi.org/10.1016/j.cej.2024.152929.

References

- M. Singh, H.M. Haverinen, P. Dhagat, G.E. Jabbour, Inkjet printing-process and its applications, Adv. Mater. 22 (2010) 673–685, https://doi.org/10.1002/ adma 200901141
- [2] N. Scoutaris, M.R. Alexander, P.R. Gellert, C.J. Roberts, Inkjet printing as a novel medicine formulation technique, J. Control. Release 156 (2011) 179–185, https://doi.org/10.1016/j.jconrel.2011.07.033.
- [3] H. Sabouri, K. Ohno, S. Perrier, Well-defined colloidal crystal films from the 2D self-assembly of core-shell semi-soft nanoparticles, Polym. Chem. 6 (2015) 7297–7307, https://doi.org/10.1039/c5py00912j.
- [4] K. Kordas, T. Mustonen, G. Toth, H. Jantunen, M. Lajunen, C. Soldano, S. Talapatra, S. Kar, R. Vajtai, P.M. Ajayan, Inkjet printing of electrically conductive patterns of carbon nanotubes, Small 2 (2006) 1021–1025, https://doi.org/10.1002/ smll.200600061.
- [5] B.-L. Huang, T.-L. Guo, S. Xu, Y. Ye, E.-G. Chen, Z.-X. Lin, Color converting film with quantum-dots for the liquid crystal displays based on inkjet printing, IEEE Photonics J. 11 (2019) 1–9, https://doi.org/10.1109/jphot.2019.2911308.
- [6] R.D. Deegan, O. Bakajin, T.F. Dupont, G. Huber, S.R. Nagel, T.A. Witten, Capillary flow as the cause of ring stains from dried liquid drops, Nature 389 (1997) 827–829, https://doi.org/10.1038/39827.
- [7] R.D. Deegan, Pattern formation in drying drops, Phys. Rev. E 61 (2000) 475, https://doi.org/10.1103/PhysRevE.61.475.
- [8] H.Y. Ko, J. Park, H. Shin, J. Moon, Rapid self-assembly of monodisperse colloidal spheres in an ink-jet printed droplet, Chem. Mater. 16 (2004) 4212–4215, https:// doi.org/10.1021/cm035256t.
- [9] D. Tian, Y. Song, L. Jiang, Patterning of controllable surface wettability for printing techniques, Chem. Soc. Rev. 42 (2013) 5184–5209, https://doi.org/10.1039/ c3cs35501b.
- [10] A.G. Marin, H. Gelderblom, A. Susarrey-Arce, A. van Houselt, L. Lefferts, J. G. Gardeniers, D. Lohse, J.H. Snoeijer, Building microscopic soccer balls with evaporating colloidal fakir drops, Proc. Natl. Acad. Sci. u.s.a. 109 (2012) 16455–16458, https://doi.org/10.1073/pnas.1209553109.
- [11] M. Dicuangco, S. Dash, J.A. Weibel, S.V. Garimella, Effect of superhydrophobic surface morphology on evaporative deposition patterns, Appl. Phys. Lett. 104 (2014), https://doi.org/10.1063/1.4878322.
- [12] D. Mampallil, H.B. Eral, D. van den Ende, F. Mugele, Control of evaporating complex fluids through electrowetting, Soft Matter 8 (2012) 10614–10617, https://doi.org/10.1039/c2sm26103k.
- [13] H.B. Eral, D.M. Augustine, M.H.G. Duits, F. Mugele, Suppressing the coffee stain effect: how to control colloidal self-assembly in evaporating drops using

- electrowetting, Soft Matter 7 (2011) 4954–4958, https://doi.org/10.1039/
- [14] S. Das, S. Chakraborty, S.K. Mitra, Ring stains in the presence of electrokinetic interactions, Phys. Rev. E 85 (2012) 046311, https://doi.org/10.1103/ PhysRevE.85.046311.
- [15] Y. Li, C. Lv, Z. Li, D. Quere, Q. Zheng, From coffee rings to coffee eyes, Soft Matter 11 (2015) 4669–4673, https://doi.org/10.1039/c5sm00654f.
- [16] M. Parsa, S. Harmand, K. Sefiane, M. Bigerelle, R. Deltombe, Effect of substrate temperature on pattern formation of nanoparticles from volatile drops, Langmuir 31 (2015) 3354–3367, https://doi.org/10.1021/acs.langmuir.5b00362.
- [17] H. Jin, J. Qian, L. Zhou, J. Yuan, H. Huang, Y. Wang, W.M. Tang, H.L. Chan, Suppressing the coffee-ring effect in semitransparent MnO₂ film for a highperformance solar-powered energy storage window, ACS Appl. Mater. Interfaces 8 (2016) 9088–9096, https://doi.org/10.1021/acsami.6b00402.
- [18] H.Y. Erbil, Control of stain geometry by drop evaporation of surfactant containing dispersions, Adv. Colloid Interface Sci. 222 (2015) 275–290, https://doi.org/ 10.1016/j.cis.2014.08.004.
- [19] V.R. Dugyala, M.G. Basavaraj, Control over coffee-ring formation in evaporating liquid drops containing ellipsoids, Langmuir 30 (2014) 8680–8686, https://doi. org/10.1021/la500803h
- [20] P.J. Yunker, T. Still, M.A. Lohr, A.G. Yodh, Suppression of the coffee-ring effect by shape-dependent capillary interactions, Nature 476 (2011) 308–311, https://doi. org/10.1038/nature10344.
- [21] M. Anyfantakis, Z. Geng, M. Morel, S. Rudiuk, D. Baigl, Modulation of the coffeering effect in particle/surfactant mixtures: the importance of particle-interface interactions, Langmuir 31 (2015) 4113–4120, https://doi.org/10.1021/acs. langmuir.5b00453.
- [22] Y. Li, Q. Yang, M. Li, Y. Song, Rate-dependent interface capture beyond the coffeering effect, Sci. Rep. 6 (2016) 24628, https://doi.org/10.1038/srep24628.
- [23] D.D. Li, L. Wang, J. Liu, Z. Huang, Manipulating nano-suspension droplet evaporation by particle surface modification, Langmuir 37 (2021) 12234–12241, https://doi.org/10.1021/acs.langmuir.1c02196.
- [24] Y.Y. Won, F.S. Bates, Nonionic block copolymer wormlike micelles, in: R. Zana, E. W. Kaler (Eds.), Giant Micelles: Properties and Applications, CRC Press, Florida, 2007, pp. 417–451.
- [25] J.F. Gohy, Block copolymer micelles, in: V. Abetz (Ed.), Block Copolymers II, Springer, Berlin, 2005, pp. 65–136.
- [26] Y.Y. Won, H.T. Davis, F.S. Bates, Molecular exchange in PEO-PB micelles in water, Macromolecules 36 (2003) 953–955, https://doi.org/10.1021/ma021439+.
- [27] D.H. Kim, A. Wei, Y.Y. Won, Preparation of super-stable gold nanorods via encapsulation into block copolymer micelles, ACS Appl. Mater. Interfaces 4 (2012) 1872–1877, https://doi.org/10.1021/am300198v.
- [28] A.C. Kamps, B.L. Sanchez-Gaytan, R.J. Hickey, N. Clarke, M. Fryd, S.J. Park, Nanoparticle-directed self-assembly of amphiphilic block copolymers, Langmuir 26 (2010) 14345–14350. https://doi.org/10.1021/la1025558.
- [29] J. Lee, N.J. Rancilio, J.M. Poulson, Y.Y. Won, Block copolymer-encapsulated CaWO₄ nanoparticles: synthesis, formulation, and characterization, ACS Appl. Mater. Interfaces 8 (2016) 8608–8619, https://doi.org/10.1021/acsami.6b00727.
- [30] M. Frounchi, S. Shamshiri, Magnetic nanoparticles-loaded PLA/PEG microspheres as drug carriers, J. Biomed. Mater. Res. A 103 (2015) 1893–1898, https://doi.org/ 10.1002/jbm.a.35317
- [31] Z.Y. Qiao, R. Ji, X.N. Huang, F.S. Du, R. Zhang, D.H. Liang, Z.C. Li, Polymersomes from dual responsive block copolymers: drug encapsulation by heating and acidtriggered release, Biomacromolecules 14 (2013) 1555–1563, https://doi.org/ 10.1021/bm400180n
- [32] Y. Wu, K. Wang, H. Tan, J. Xu, J. Zhu, Emulsion solvent evaporation-induced self-assembly of block copolymers containing pH-sensitive block, Langmuir 33 (2017) 9889–9896. https://doi.org/10.1021/acs.langmuir.7b02330.
- [33] M. Heskins, J.E. Guillet, Solution properties of poly(N-isopropylacrylamide), J. Macromol. Sci.-Chem. 2 (1968) 1441–1455, https://doi.org/10.1080/ 10601326808051910
- [34] Y. Tsuboi, Y. Yoshida, K. Okada, N. Kitamura, Phase separation dynamics of aqueous solutions of thermoresponsive polymers studied by a laser T-jump technique, J. Phys. Chem. B 112 (2008) 2562–2565, https://doi.org/10.1021/ ip711128s.
- [35] K.N. Plunkett, X. Zhu, J.S. Moore, D.E. Leckband, PNIPAM chain collapse depends on the molecular weight and grafting density, Langmuir 22 (2006) 4259–4266, https://doi.org/10.1021/la0531502.
- [36] J. Zhang, R. Pelton, Poly(N-isopropylacrylamide) microgels at the air-water interface, Langmuir 15 (1999) 8032–8036, https://doi.org/10.1021/la9903160.
- [37] T. Still, P.J. Yunker, K. Hanson, Z.S. Davidson, M.A. Lohr, K.B. Aptowicz, A. G. Yodh, Temperature-sensitive hydrogel-particle films from evaporating drops, Adv. Mater. Interfaces 2 (2015) 1500371, https://doi.org/10.1002/admi.201500271
- [38] K. Horigome, D. Suzuki, Drying mechanism of poly(N-isopropylacrylamide) microgel dispersions, Langmuir 28 (2012) 12962–12970, https://doi.org/ 10.1021/la302465w
- [39] M. Mayarani, M.G. Basavaraj, D.K. Satapathy, Viscoelastic particle-laden interface inhibits coffee-ring formation, Langmuir 34 (2018) 14294–14301, https://doi.org/ 10.1021/acs.langmuir.8b02739.
- [40] T. Tang, V. Castelletto, P. Parras, I.W. Hamley, S.M. King, D. Roy, S. Perrier, R. Hoogenboom, U.S. Schubert, Thermo-responsive poly(methyl methacrylate)block-poly(N-isopropylacrylamide) block copolymers synthesized by RAFT polymerization: micellization and gelation, Macromol. Chem. Phys. 207 (2006) 1718–1726, https://doi.org/10.1002/macp.200600309.

- [41] L.-P. Wang, Y.-P. Wang, X.-W. Pei, B. Peng, Synthesis of poly(methyl methacrylate)-b-poly(N-isopropylacrylamide) (PMMA-b-PNIPAM) amphiphilic diblock copolymer brushes on halloysite substrate via reverse ATRP, React. Funct. Polym. 68 (2008) 649–655, https://doi.org/10.1016/j. reactfunctpolym.2007.10.034.
- [42] R.B. Grubbs, Roles of polymer ligands in nanoparticle stabilization, Polym. Rev. 47 (2007) 197–215, https://doi.org/10.1080/15583720701271245.
- [43] J.Y. Choi, C.H. Park, J. Lee, Effect of polymer molecular weight on nanocomminution of poorly soluble drug, Drug Deliv. 15 (2008) 347–353, https:// doi.org/10.1080/10717540802039113.
- [44] J.Y. Lee, J.W. Hwang, H.W. Jung, S.H. Kim, S.J. Lee, K. Yoon, D.A. Weitz, Fast dynamics and relaxation of colloidal drops during the drying process using multispeckle diffusing wave spectroscopy, Langmuir 29 (2013) 861–866, https:// doi.org/10.1021/la3046059.
- [45] G.J. Oh, J.W. Hwang, K.W. Bong, H.W. Jung, S.J. Lee, Particle dynamics and relaxation in bimodal suspensions during drying using multispeckle diffusing wave spectroscopy, AIChE J. 63 (2016) 1114–1121, https://doi.org/10.1002/aic.15437.
- [46] J.I. Amalvy, C.A. Lasquibar, R. Arizaga, H. Rabal, M. Trivi, Application of dynamic speckle interferometry to the drying of coatings, Prog. Org. Coat. 42 (2001) 89–99, https://doi.org/10.1016/S0300-9440(01)00160-6.
- [47] R. Arizaga, M. Trivi, H. Rabal, Speckle time evolution characterization by the cooccurence matrix analysis, Opt. Laser Technol. 31 (1999) 163–169, https://doi. org/10.1016/S0030-3992(99)00033-X.
- [48] R. Arizaga, E.E. Grumel, N. Cap, M. Trivi, J.I. Amalvy, B. Yepes, G. Ricaurte, Following the drying of spray paints using space and time contrast of dynamic speckle, J. Coat. Technol. Res. 3 (2006) 295–299, https://doi.org/10.1007/ s11998-006-0025-2.
- [49] B.S. Park, W.-G. Ahn, K.I. Jung, S.J. Lee, K.-Y. Lee, H.W. Jung, Analysis of the drying behavior of suspension drops with spherical and ellipsoidal particles, Dry. Technol. 36 (2018) 2022–2029, https://doi.org/10.1080/ 07373937 2018 1433684
- [50] S. Kulkeratiyut, S. Kulkeratiyut, F.D. Blum, Bound carbonyls in PMMA-adsorbed on silica using transmission FTIR, J. Polym. Sci. b: Polym. Phys. 44 (2006) 2071–2078, https://doi.org/10.1002/polb.20871.
- [51] R.R. Madathingal, S.L. Wunder, Effect of particle structure and surface chemistry on PMMA adsorption to silica nanoparticles, Langmuir 26 (2010) 5077–5087, https://doi.org/10.1021/la903505y.
- [52] E. Burdukova, N. Ishida, T. Shaddick, G.V. Franks, The size of particle aggregates produced by flocculation with PNIPAM, as a function of temperature, J. Colloid Interface Sci. 354 (2011) 82–88, https://doi.org/10.1016/j.jcis.2010.10.016.
- [53] J. Brijitta, B.V. Tata, T. Kaliyappan, Phase behavior of poly(N-isopropylacrylamide) nanogel dispersions: temperature dependent particle size and interactions, J. Nanosci. Nanotechnol. 9 (2009) 5323–5328, https://doi.org/10.1166/jnn.2009.1144.
- [54] M. Karg, S. Wellert, S. Prevost, R. Schweins, C. Dewhurst, L.M. Liz-Marzán, T. Hellweg, Well defined hybrid PNIPAM core-shell microgels: size variation of the silica nanoparticle core, Colloid Polym. Sci. 289 (2010) 699–709, https://doi.org/ 10.1007/sp0396-010-2337-2
- [55] W.F. Claussen, Surface tension and surface structure of water, Science 156 (1967) 1226–1227, https://doi.org/10.1126/science.156.3779.1226.
- [56] C. Zhang, W. Chen, Y. Hong, X. Wang, Surface activity and structure of temperature-responsive polymer surfactants based on PNIPAm at the air/solution interface, Langmuir 37 (2021) 4632–4638, https://doi.org/10.1021/acs. langmuir_1c00320.
- [57] L.T. Lee, B. Jean, A. Menelle, Effect of temperature on the adsorption of poly(N-isopropylacrylamide) at the air-solution interface, Langmuir 15 (1999) 3267–3272, https://doi.org/10.1021/la981531s.
- [58] A. Maestro, D. Jones, C. Sánchez de Rojas Candela, E. Guzman, M.H. Duits, P. Cicuta, Tuning interfacial properties and processes by controlling the rheology and structure of poly(*N*-isopropylacrylamide) particles at air/water interfaces, Langmuir 34 (2018) 7067–7076, https://doi.org/10.1021/acs.langmuir.7b03879.
- [59] S.H. Kim, G.W. Lee, B. Chun, K.-Y. Lee, H.W. Jung, Rheological behavior and drying characteristics of ceria-based suspensions under various pH conditions, Powder Technol. 412 (2022) 117984, https://doi.org/10.1016/j. powtec 2022 117984
- [60] Y. Lee, S.H. Kim, S.J. Lee, J. Bang, H.W. Jung, Light-scattering analysis of drying behavior in suspension droplets with silica and polystyrene particles and a hydrosoluble polymer, Langmuir 39 (2023) 17222–17231, https://doi.org/ 10.1021/acs.langmuir.3c02280.
- [61] Y. Ooi, I. Hanasaki, D. Mizumura, Y. Matsuda, Suppressing the coffee-ring effect of colloidal droplets by dispersed cellulose nanofibers, Sci. Technol. Adv. Mater. 18 (2017) 316–324, https://doi.org/10.1080/14686996.2017.1314776.
- [62] R. Bhardwaj, X. Fang, P. Somasundaran, D. Attinger, Self-assembly of colloidal particles from evaporating droplets: role of DLVO interactions and proposition of a phase diagram, Langmuir 26 (2010) 7833–7842, https://doi.org/10.1021/ 129047227
- [63] L.J. Mendoza-Herrera, D.C. Schinca, L.B. Scaffardi, E.E. Grumel, M. Trivi, Measurement of latex microparticle size by dynamic speckle technique, Opt. Laser Eng. 140 (2021) 106528, https://doi.org/10.1016/j.optlaseng.2020.106528.

- [64] L. Xu, S. Davies, A.B. Schofield, D.A. Weitz, Dynamics of drying in 3D porous media, Phys. Rev. Lett. 101 (2008) 094502, https://doi.org/10.1103/ PhysRevLett.101.094502.
- [65] P. Xu, A.S. Mujumdar, B. Yu, Drying-induced cracks in thin film fabricated from colloidal dispersions, Dry. Technol. 27 (2009) 636–652, https://doi.org/10.1080/ 07373930902820804.
- [66] B. Wang, W. Zhang, W. Zhang, A.S. Mujumdar, L. Huang, Progress in drying technology for nanomaterials, Dry. Technol. 23 (2005) 7–32, https://doi.org/ 10.1081/drt-200047900.